Independent constraints on deep-sea temperatures across two early Eocene hyperthermals from clumped isotope thermometry

Authors: Tobias Agterhuis[1*], Martin Ziegler[1], Niels J. de Winter[1,2] & Lucas J. Lourens[1]

Affiliations: [1]Department of Earth Sciences, Faculty of Geosciences, Utrecht University, Utrecht, the Netherlands

[2]AMGC research group, Vrije Universiteit Brussel, Brussels, Belgium

*Corresponding author. Email: t.agterhuis@uu.nl.

Abstract

The early Eocene hothouse experienced the occurrence of transient global warming events, so-called hyperthermals. The deep ocean constitutes a stable and vast heat reservoir, and hence arguably provides a good estimate of the global mean climate state. However, available proxy deep-sea temperature reconstructions rely on uncertain assumptions of non-thermal influences associated with seawater chemistry and species-specific effects. Here, we apply carbonate clumped isotope thermometry on benthic foraminifera to evaluate South Atlantic deep-sea temperatures across two early Eocene hyperthermal events. Our reconstructions indicate deep-sea temperatures of 13.5±1.8 °C (95% CI) for the background state, and average hyperthermal peak temperatures of 16.9±2.2 °C (95% CI). Absolute temperatures are approximately three degrees warmer than estimates from benthic oxygen isotopes. These findings imply a necessary reassessment of the isotope composition of ocean water during the Eocene, of deep-sea pH in hothouse climates, and of a potential pH effect on benthic foraminiferal oxygen isotope records.

The early Eocene (56-48 Ma) was the warmest period of the Cenozoic, characterized by very high CO_2 levels (~600-2500 ppm)[1,2], reduced latitudinal temperature gradients, and absence of continental ice sheets[3–10]. As such, the early Eocene hothouse is considered as a potential analogue for our future climate[11]. The deep ocean is a relatively stable component in the climate system because of its high heat capacity, and therefore provides information on the state of the global mean climate[12–15].

Much of our understanding of the early Eocene climate state and variability is based on deep-sea temperature estimates derived from benthic foraminiferal oxygen isotopes ($\delta^{18}O_b$)[3,10]. For instance, negative excursions in high-resolution stable oxygen and carbon isotope records have revealed the periodic occurrence of multiple transient (10–100 kyr) episodes of global warming and ocean acidification (hyperthermal events; e.g. PETM, ETM2 and

ETM3)[16–19], generally linked to massive release of isotopically light carbon into the ocean-atmosphere system[16,20–22].

The reliability of using $\delta^{18}O_b$ for temperature reconstructions is however hampered by uncertainties in nonthermal factors. Apart from temperature, this proxy depends on the $\delta^{18}O$ composition of the seawater ($\delta^{18}O_{sw}$), which is poorly constrained for the Earth's past[23,24]. The traditional view is that with the absence of major ice sheets in the Eocene, a fixed ice-free $\delta^{18}O_{sw}$ value can be applied to convert the $\delta^{18}O_b$ values into deep-sea temperatures[3,4,25]. Yet, in this approach, other factors, such as deep water mass properties (salinity), are generally ignored as potential sources that could have affected the $\delta^{18}O_{sw}$ composition[23,24]. Furthermore, it is known that changes in seawater pH and species-specific physiological factors may alter $\delta^{18}O_b$, which complicate the use of oxygen isotopes in reconstructing ocean temperature[23,24,26–29].

To overcome these uncertainties, early Eocene deep-sea temperature reconstructions have been obtained from benthic foraminiferal Mg/Ca ratios[12,30–31]. While this temperature proxy has the advantage that it is not influenced by the $\delta^{18}O_{sw}$ composition, it depends on the other hand on the Mg/Ca composition of the seawater (Mg/Ca_{sw})[31,32]. This ratio in the ocean appears to have varied on long time scales (>1 Myr) in the geological past[33–35], and lack of sufficient knowledge on these past changes introduce significant uncertainty in temperature estimates[31–36]. Similar to $\delta^{18}O$, the Mg/Ca proxy is also affected by the carbonate chemistry of the ocean and vital effects that require species-specific calibrations[34,37–42]. Deep-sea temperature reconstructions based on $\delta^{18}O_b$ and Mg/Ca are therefore not as robust as commonly appreciated.

The carbonate clumped isotope thermometer (Δ_{47}) shows great potential to improve temperature reconstructions as it is insensitive to the isotope composition of the seawater and largely unaffected by pH and physiological factors[43–50]. This proxy uses the temperature dependence of the degree of bonding of two heavy rare isotopes (^{13}C and ^{18}O) within the carbonate ion, with more clumping favored at colder temperatures[51–53]. Recent analytical developments now ensure inter-laboratory consistency of measurements[54,55] and allow analysis of relatively small samples sizes (e.g. foraminifera)[54–59]. These advances in the clumped isotope proxy enable reconstruction of marine temperatures independent from non-thermal uncertainties[60–66]. So far, application of Δ_{47} on the relatively cooler Miocene and middle Eocene have revealed a much warmer deep ocean than traditionally accepted[63,65–67], raising the question whether other periods in the Cenozoic also experienced warmer deep-sea temperatures than assumed.

Here, we report the first Δ_{47}-based deep-sea temperature estimates across two early Eocene hyperthermal events, namely Eocene Thermal Maximum 2 (ETM2 or H1) and H2 (~54.1 and 54.0 Ma respectively), that occurred approximately 2 Myrs after the Paleocene-Eocene Thermal Maximum (PETM)[68,69]. High-resolution (~1 kyr) benthic foraminiferal carbon and oxygen isotope records were previously generated from four ODP Sites (1262, 1263, 1265 and 1267) at the Walvis Ridge and one site at Maud Rise in the Weddell Sea (ODP Site 690)[69] with paleowater depths ranging from ~1500 m to ~3600 m (refs 70,71) (Extended Data Fig. 1). The $\delta^{18}O_b$ records of all these sites

show almost identical values, suggesting that they reflect similar deep-sea conditions[69]. Here, we revisited these sites and applied paired stable and clumped isotope analyses on the benthic foraminiferal species *Nuttallides truempyi* and *Oridorsalis umbonatus* for confident reconstruction of deep-sea temperatures in the South Atlantic across these two hyperthermals.

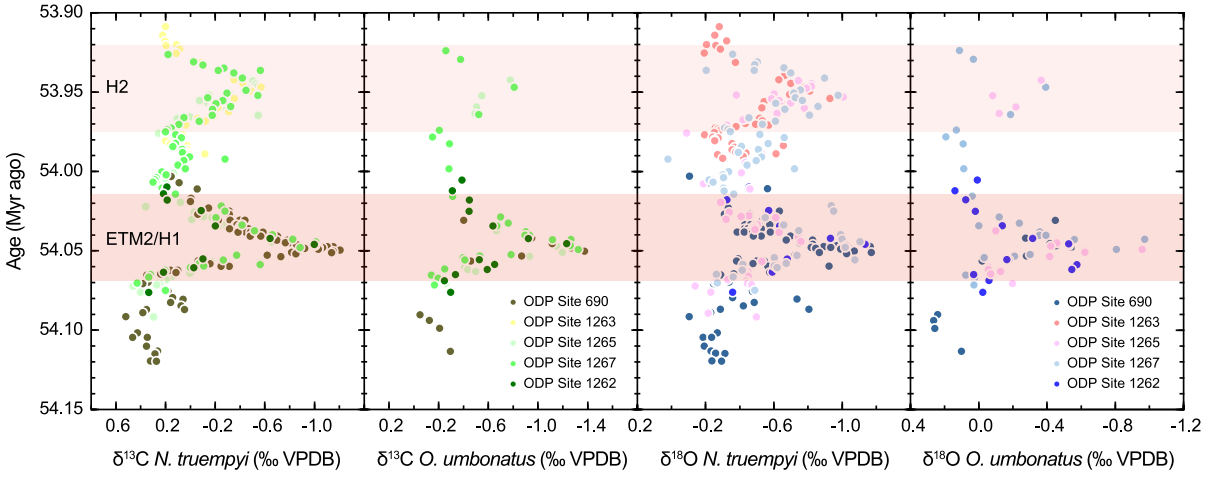

Fig. 1 | South Atlantic benthic foraminiferal $\delta^{13}C$ and $\delta^{18}O$ records across ETM2 and H2. This figure shows the $\delta^{13}C$ and $\delta^{18}O$ measurements for benthic foraminifera *N. truempyi* and *O. umbonatus*. The apparent offset in the stable isotopes between the two species indicates different isotope fractionation[29]. The ODP Sites from the Walvis Ridge used for benthic foraminiferal stable and clumped isotope analysis include Sites 1262, 1263, 1265 and 1267. Paleowater depth ranges from ~1500 m (Site 1263) to ~3600 m (Site 1262)[71]. Maud Rise is represented by ODP Site 690 with a paleowater depth of ~2100 m)[70]. The stable isotope data is plotted against age following the age models of refs 69, 105.

Results and discussion

Stable and clumped isotope analysis. Our new carbon and oxygen isotope measurements (Fig. 1) are consistent with the previously published benthic $\delta^{13}C_b$ and $\delta^{18}O_b$ records[69]. Prominent negative excursions in $\delta^{13}C_b$ (–1.4‰ and –0.8‰, respectively) and $\delta^{18}O_b$ (–0.8‰ and –0.5‰ respectively) characterize ETM2 and H2, showing ETM2 is the most prominent event. These negative $\delta^{13}C_b$ and $\delta^{18}O_b$ excursions indicate the injection of large amounts of ^{13}C-depleted carbon into the climate system and elevated deep-sea temperatures respectively[68,69]. Limited isotope data is obtained for the peak ETM2 interval at the Walvis Ridge sites, as benthic foraminifera are rare and small-sized in the associated red clay layer, known as the Elmo horizon[68,69].

Due to the sporadic natural abundance of ^{13}C–^{18}O bonds within carbonate ions[51–53], clumped isotope analysis requires large samples to achieve high analytical precision, which is required in paleoclimate reconstructions[54,58,59]. Averaging of numerous replicate Δ_{47} measurements (~2–3 mg, each replicate ~100 µg) is required to mitigate large analytical uncertainty[54,58,59]. The strategy of averaging Δ_{47} measurements for precise reconstruction of small temperature variability becomes especially important when sample size is limited[72]. In our study, the abundance of

93 *N. truempyi* and *O. umbonatus* is too low in the samples at all sites to undertake enough measurements for the
94 precise reconstruction of deep-sea temperature change across ETM-2 and H2. As a solution to obtain the desired
95 precision (<3°C at 95% confidence interval), we sorted the Δ_{47} measurements from all sites based on their
96 corresponding $\delta^{18}O_b$ values and compiled three average clumped isotope temperatures that represent the average
97 background state (high $\delta^{18}O_b$), average slope (middle $\delta^{18}O_b$), and average hyperthermal peak (low $\delta^{18}O_b$) conditions
98 across the studied interval. So instead of showing deep-sea temperatures in a time series, we plotted three clumped
99 isotope temperature bins that are representative for three different climate states. A Welch's t-test was performed
100 between the 'high $\delta^{18}O_b$' and 'low $\delta^{18}O_b$' Δ_{47} measurements to obtain the most optimal bin size for the background
101 and hyperthermal temperatures[72] (Extended Data Table 1 and Extended Data Fig. 2).
102
103 **Deep-sea temperatures.** Our Δ_{47}-based reconstruction indicates very warm deep waters with average background
104 temperatures of 13.5±1.8 °C (95% CI; analytical uncertainty) and average hyperthermal peak temperatures of
105 16.9±2.2 °C (95% CI) (Fig. 2b; see Extended Data Fig. 3 for temperatures per site). The true peak temperature of
106 ETM2 is expected to be even warmer due to the smoothing effect that results from averaging of Δ_{47} data and the
107 limited measurements derived from the Elmo horizon. This expected elevated temperature is also indicated by the
108 magnitude of the stable isotope excursion, which is much larger (~150%) than that of H2 (ref 69) (Fig. 2b).
109

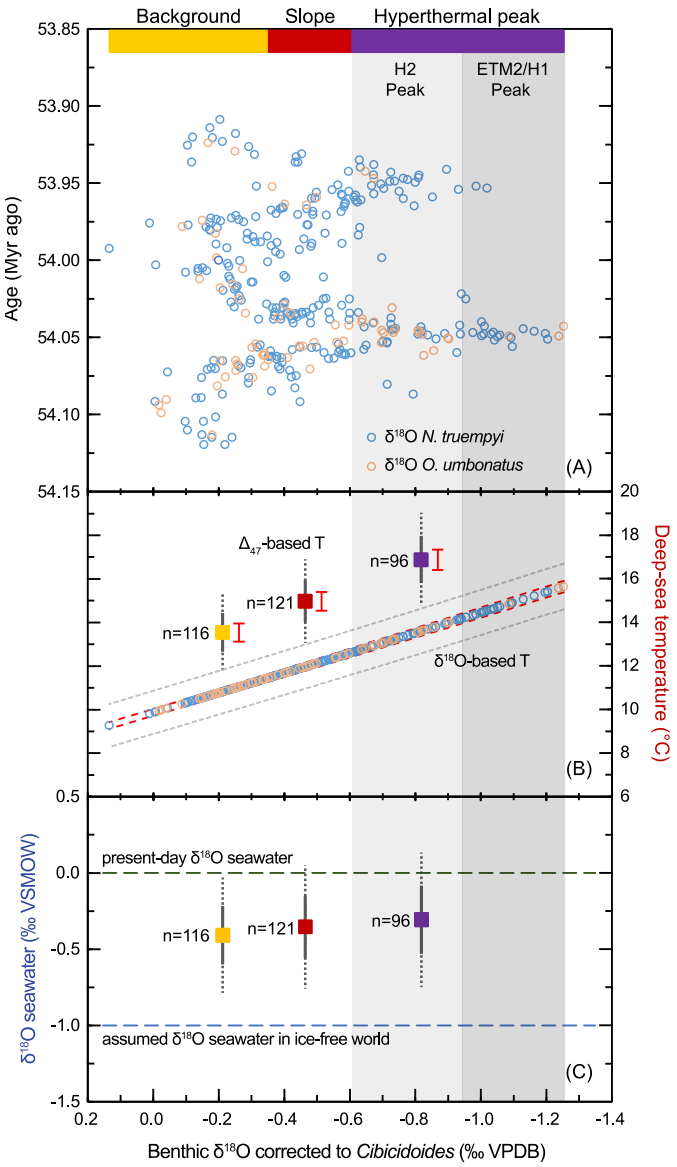

Fig. 2 | Deep-sea temperatures and $\delta^{18}O$ seawater composition. a, $\delta^{18}O_b$ values derived from *N. truempyi* and *O. umbonatus* that are corrected towards *Cibicidoides* (for seawater equilibrium) across ETM2 and H2. **b**, Deep-sea temperatures based on Δ_{47} and $\delta^{18}O_b$ across ETM2 and H2. The yellow (background), red (slope), and purple (hyperthermal peak) bars indicate the range in $\delta^{18}O_b$ values that correspond to the Δ_{47} measurements used for compiling these three bins. The dark grey error bars on the Δ_{47}-based temperatures represent the analytical uncertainty (68% and 95% CI). The additional red bars indicate the uncertainty (95% CI) of the calibration of ref 49. The striped grey and red envelopes on the $\delta^{18}O_b$-based deep-sea temperatures display the analytical uncertainty (two times the long-term SD of the IAEA-C2 standard) and the uncertainty (95% CI) of the calibration of ref 79 respectively. Overall, the uncertainty is dominated by the spread in the measurements, and is only influenced to a minor extent by the calibration uncertainties. **c**, $\delta^{18}O_{sw}$ across the ETM2 and H2 interval, which we calculated by using the Δ_{47}-based temperatures in combination with the $\delta^{18}O_b$ values in the oxygen isotope-temperature relationship of ref 79 (Methods). The error bars indicate the analytical uncertainty derived from the precision of the Δ_{47}-based temperatures and $\delta^{18}O_b$ measurements. The dashed lines show the assumed $\delta^{18}O_{sw}$ value based on ice-free conditions and the present-day icehouse $\delta^{18}O_{sw}$ value.

Our background temperatures are in broad agreement with early Eocene low-resolution reconstructions from Mg/Ca. These Mg/Ca-based records however indicate a range of possible deep-sea temperatures, i.e. between 10 to ~15 °C, associated with major uncertainty in Mg/Ca_{sw} ratios prior to the middle Eocene[31,36]. To compare the clumped isotope-based deep-sea temperatures with those derived from $\delta^{18}O_b$ estimates, we use the same approach as applied in the revised deep-sea temperature compilation from $\delta^{18}O_b$ of ref[31]. Traditionally, it is common practice in paleoceanography (e.g. ref 3) to apply the classic $\delta^{18}O$-temperature relationship of ref[73], which assumes that the oxygen isotopes of modern *Oridorsalis* are in equilibrium with the seawater isotope composition based on core top data[73–76]. *Cibicidoides* is the foraminiferal genus mostly used for deep ocean reconstructions[3], and is usually corrected for seawater equilibrium since it was found that this genus has an 0.64‰ offset in $\delta^{18}O_b$ with *Oridorsalis*[73–76]. However, more extensive recent studies show evidence that modern *Cibicidoides* are in close isotopic equilibrium with seawater and derive a $\delta^{18}O$-temperature relationship from this genus[77–79]. To calculate early Cenozoic deep-sea temperatures from other foraminiferal species with this approach, well-documented correction factors are used to account for interspecies $\delta^{18}O_b$ offsets with *Cibicidoides*[29,31]. In Fig. 2b, we adjusted the *N. truempyi* and *O. umbonatus* $\delta^{18}O_b$ values towards *Cibicidoides* and subsequently calculated deep-sea temperatures from these values following ref 79 (Methods). For the mean $\delta^{18}O_{sw}$ of global ocean, we adopted a fixed value of −1 ‰ VSMOW based on the assumption of absence of continental ice in the early Eocene[25]. In comparison to the $\delta^{18}O$-based deep-sea temperatures, our clumped isotope reconstructions are on average three degrees warmer, i.e., 13.5±1.8 °C (95% CI) versus 10.8±1.0 °C (2 SD) for background, 15.0±1.9 °C (95% CI) versus 12.0±1.0 °C (2 SD) for slope, and 16.9±2.2 °C (95% CI) versus 13.6±1.0 °C (2 SD) for average hyperthermal peak temperatures (Fig. 2b). Note that if we would instead apply the traditional $\delta^{18}O$-temperature calibration of ref 73 and assuming *Oridorsalis* $\delta^{18}O_b$ representing equilibrium, the temperature difference between clumped isotopes and oxygen isotopes is larger as the $\delta^{18}O$-based temperatures become ~1–2 °C colder using that approach.

Constraints on Early Eocene seawater oxygen isotope composition. An important consequence of the warmer Δ_{47}-derived deep-sea temperatures for the early Eocene is that they imply a mean value for deep water $\delta^{18}O_{sw}$ of approximately –0.35±0.4‰ VSMOW (95 % CI), which is a much higher value than usually assumed (Fig. 2c; Methods). Several factors may explain this deviation. Firstly, substantial continental ice sheets (about half the size of present-day) may have existed during the early Eocene. However, this hypothesis is unlikely given that subtropical temperatures and vegetation prevailed at both poles[80,81]. Though small ephemeral ice caps may have been present in Antarctica and in the Arctic region, records of ice rafted debris show that significant high-latitude ice formation was not initiated prior to the middle Eocene[82–84].

Secondly, the deep Atlantic basin may have been filled with more saline waters during the early Eocene, perhaps originating from the lower latitude sea surface through evaporation dominated deep-water formation[85]. However, a complicating factor is that other regions of the deep ocean must have had a much lighter $\delta^{18}O_{sw}$ (fresher waters) to

158 balance the global ocean $\delta^{18}O_{sw}$ towards ice-free conditions. Such large spatial differences in deep-sea $\delta^{18}O_{sw}$ are
159 difficult to reconcile with small isotope gradients between ocean basins in the early Eocene[86] and considering the
160 relatively uniform distribution of $\delta^{18}O_{sw}$ values in the modern ocean.

161 Finally, large-scale groundwater storage on land and crustal isotope interaction by seafloor spreading rates may
162 have affected the global ocean $\delta^{18}O_{sw}$ composition. Much like ice sheets, large aquifers filled with isotopically light
163 water would change the ocean $\delta^{18}O_{sw}$ towards heavier values[87,88]. Is has been hypothesized that charging of these
164 groundwater reservoirs could explain the apparent large sea level fluctuations (tens of meters) in the hothouse
165 climate of the Cretaceous[87,88]. However, geological evidence is not available and climate models have not yet been
166 able to confirm the existence of these large aquifers in warm climates[89]. On million-year time scales, the ocean
167 $\delta^{18}O_{sw}$ composition may also change through the isotopic exchange of ocean water cycling through the oceanic
168 crust[90,91]. The classic idea that seafloor spreading decreased over the past ~100 Myrs (ref 92) is contradicted by
169 more recent reconstructions[93]. Despite these new studies do not reveal any trend, they though indicate large
170 fluctuations in seafloor spreading rates[93] that may have altered the $\delta^{18}O_{sw}$ composition[90,91]. In summary, several
171 factors could explain elevated deep-sea $\delta^{18}O_{sw}$ values. However, our current understanding does not point towards
172 one explanation as the most probable, and it remains possible that our observations result from a combination of
173 these factors.
174
175 **Potential pH effect on $\delta^{18}O_b$ and species-specific isotope fractionation.** Alternatively, factors besides an
176 underestimation of $\delta^{18}O_{sw}$ may also explain the cold temperature bias of the $\delta^{18}O_b$. On top of temperature and
177 $\delta^{18}O_{sw}$, the oxygen isotope compositions of foraminifera are also influenced by pH and vital effects[23,24,26–29]. The
178 assumed $\delta^{18}O_{sw}$ value of −1 ‰ VSMOW may be correct if a pH effect on the incorporation of the oxygen isotopes
179 in the foraminiferal skeleton is taken into account[26–28]. The hothouse of the early Eocene, associated by highly
180 elevated atmospheric CO_2 levels[1,2], was probably characterized by low pH in the global ocean. Though absolute
181 pH reconstructions of the deep-sea are not available, the early Eocene deep-sea pH may have been ~0.4 units
182 lower than modern times based on combined proxy-model and model studies[94,95]. Both culture experiments and
183 field studies have shown that foraminiferal $\delta^{18}O_b$ is sensitive to pH. Decreasing pH generally cause increasing $\delta^{18}O_b$
184 values, but with the magnitude of this effect varies among species[26]. In theory, clumped isotopes should also be
185 affected by pH to some extent, but this effect is found to be much smaller than on oxygen isotopes[96,97]. A pH effect
186 on $\delta^{18}O_b$ has been successfully demonstrated for planktic foraminifera[26], yet it is uncertain whether this effect also
187 exists in benthic foraminifera[79]. Notwithstanding, the underestimated early Eocene deep-sea temperatures
188 indicated by $\delta^{18}O_b$ are consistent with a scenario of highly reduced sea water pH.

189 In addition to a potential pH effect, uncertainties and changes in species-specific isotope fractionation on
190 geological time scales are also important to consider as a possible explanation for the relatively cold $\delta^{18}O_b$-based
191 deep-sea temperatures. While core top and deep time studies suggest that species-specific effects do not influence

192 the Δ_{47} composition of foraminifera[43,45,47–49,61,66], offsets in $\delta^{18}O_b$ are evident among different foraminiferal
193 species[29,76]. These interspecies offsets in $\delta^{18}O_b$ (and $\delta^{13}C_b$) also appear to change of over time. For instance, a
194 $\delta^{18}O_b$ offset of 0.64 ‰ is recorded between *Cibicidoides/Planulina* and *Oridorsalis* for the late Cenozoic, while this
195 offset is different in the early Cenozoic, i.e. 0.28 ‰[29,76]. These changing isotopic offsets may suggest that vital
196 effects were not constant over the Cenozoic. These offsets are difficult to quantify, considering the evolutionary and
197 (probably also species-specific) pH effects on $\delta^{18}O_b$ that may have played a role through geological time[29].
198 Therefore, it is complicated to establish an assumed species oxygen isotope equilibrium value in deep time with
199 certainty. Other problems arise from the fact that there seems to be no commonly accepted view on which modern
200 benthic foraminiferal species precipitate their tests in equilibrium with seawater and the application on absolute
201 deep-sea temperature reconstructions, which becomes evident from Cenozoic deep-sea temperature compilations
202 that apply contrasting methods[3,10,31].
203
204 **Deep-sea warming during hyperthermal events.** Considering our reconstructed background and average
205 hyperthermal peak temperatures (13.5±1.8 °C and 16.9±2.2 °C respectively), clumped isotopes indicate an average
206 hyperthermal deep-sea warming of 3.4±2.8 °C (95% CI). When taking into account a pH effect on $\delta^{18}O_b$, oxygen
207 isotope thermometry may underestimate deep-sea warming during hyperthermals, as a further acidification of the
208 deep water is expected from numerical models (in absence of deep-sea pH proxy reconstructions)[95]. The effect of
209 an even lower pH would result in a dampening of the negative $\delta^{18}O_b$ excursion of these warming events to almost
210 half of the original magnitude, resulting in an significant underestimation of the deep-sea warming[95]. While the deep-
211 sea warming from Δ_{47} and $\delta^{18}O_b$ in our reconstructions seems to be fairly similar (Fig. 2b), we note that the
212 temperature uncertainty in the clumped isotope temperatures does allow the possibility that the true deep-sea
213 temperature change is larger than indicated by $\delta^{18}O_b$. Future efforts to investigate pH effects in benthic foraminifera
214 as well as a larger coverage of clumped isotope based reconstructions may provide more definite constraints on
215 the effect of pH on deep-sea temperature reconstructions from oxygen isotopes.
216 Hyperthermal deep-sea temperature reconstructions based on Mg/Ca are currently only available for the PETM
217 and indicate 4–5 °C warming[30]. The average deep-sea warming of 3.4±2.8 °C (95% CI) we estimate for ETM2-H2
218 is significantly higher than the warming one may would expect, since the average oxygen isotopic excursion of
219 ETM2-H2 of 0.6‰ (Fig. 2a) is about one quarter the size of that of the PETM (i.e. 2.5‰)[68,69,98]. This discrepancy
220 implies that either the current Mg/Ca-based temperatures largely underestimate the deep-sea warming during the
221 PETM or that the relative magnitude of the oxygen isotope excursion derived from the benthic foraminifera between
222 ETM2-H2 and PETM cannot be simply extrapolated in terms of temperature. Secular changes in Mg/Ca_{sw} are likely
223 to act on much longer time scales than hyperthermal variability[32], and this underestimation of deep-sea temperature
224 variability by Mg/Ca in the Eocene may potentially result from a lowering of the Mg/Ca-temperature sensitivity at
225 low Mg/Ca_{sw} values[42]. Deep-sea temperature reconstructions of the PETM and/or ETM2 based on both clumped

isotopes and Mg/Ca are needed to test this Mg/Ca sensitivity. Alternatively, Mg/Ca-based deep-sea warming of the PETM may be accurate when the ETM2-H2 and PETM were characterized by a similar magnitude of deep-sea warming despite their very different $\delta^{18}O_b$ excursions. The large negative $\delta^{18}O_b$ excursion of the PETM could contain a large contribution of a change in $\delta^{18}O_{sw}$, namely a switch to a much fresher water mass during the event[30]. However, numerical models contradict such a scenario and find instead a reduction in deep water formation in the high-latitude Southern Ocean and initiation of source regions in the saline surface waters of the Tethys Ocean during the PETM[85].

Conclusions and further implications. In short, our study suggests that confident marine temperature reconstructions based on oxygen isotope thermometry can only be achieved with independent constrains on non-thermal effects. Without these constraints, the reliability of the classic reconstructions of the early Eocene[3,10,31] should be questioned. Our findings corroborate similar findings in other periods of the Cenozoic, such as the Miocene[65–67]. These findings clearly warrant a revision of the traditional Cenozoic history of deep-sea temperatures that has provided us with a presumed benchmark of our understanding of global climate evolution over the past 66 Myrs[3,10,31].

Finally, our warmer temperatures may have implications for estimates of climate sensitivity in the early Eocene if we assume that our reconstructed South Atlantic deep-sea temperatures are representative for the global deep ocean. Available middle Eocene (~43 Ma) Atlantic Δ_{47}-based reconstructions from multiple sites already indicate almost identical deep-sea temperatures between the North and South Atlantic[63]. Reconstructions from the other ocean basins (e.g. Pacific) are needed to further test our assumption of globally uniform deep-sea temperatures in the Eocene. Yet, if the early Eocene global deep ocean was warmer on a global scale than previously thought, these warmer temperatures would result in higher estimates of global mean temperatures and climate sensitivity than previously obtained from $\delta^{18}O_b$ studies[9,14]. Such higher estimates would be in better agreement with constraints from sea surface temperature reconstructions[2,9]. Through providing independent and accurate temperature reconstructions, the clumped isotope proxy opens up new opportunities to investigate the distribution of different water masses in the ocean basins and test the existing views on the homogeneity/heterogeneity of the ocean over the Cenozoic.

Methods

Foraminiferal preservation and sampling. We performed stable and clumped isotope measurements on monospecific multi-specimen samples of *Nuttallides truempyi* and *Oridorsalis umbonatus*, which were picked from the >212 µm sediment size fractions of the samples of ref 69. Grouping Δ_{47} measurements from different benthic species together to produce one temperature estimate requires the assumption of absence of foraminiferal species-specific effects on Δ_{47}, which is supported by both modern core top and deep time studies[43,45,47–49,61,66]. Scanning

electron microscope (SEM) images were previously generated to examine the preservation throughout the studied interval and indicate that the foraminiferal tests are moderately altered by recrystallization/secondary calcite[69]. Nevertheless, the effect of recrystallization of primary calcite on the Δ_{47} signal in benthic foraminifera has been shown to be largely negligible[63,66,99], since this diagenesis usually occurs during early burial[100–102], and therefore records similar temperatures as the seafloor temperatures. Due to limiting numbers of picked foraminifera per sample, we needed to pool foraminifers from neighboring samples to obtain sufficient foraminiferal material (~25 specimens per measurement), which resulted in averaging in the depth domain. Prior to isotope analysis, foraminiferal samples were cleaned by removing adherent contaminants, for instance nannofossils, organics and clay particles. The foraminifers were gently cracked between two glass plates to enable any chamber infill to escape, and subsequently ultrasonicated in deionized water at least two times for 20 seconds. The test fragments were rinsed until the suspended particles were removed (at least two times after one ultrasonication), and oven-dried at 40 °C for one night.

Clumped isotope analysis. In total, 333 successful stable and clumped isotope sample measurements were generated across the ETM2 and H2 interval. Our analytical methods generally follow the methodology reported in previous work[54–59], and a more detailed description can be found in the Supplementary Information. We performed measurements of ~100 µg foraminiferal material each on a *Thermo Scientific Kiel IV* (Thermo Fisher Scientific, Waltham, MA, USA) carbonate preparation device coupled to a *Thermo Scientific MAT 253 Plus* mass spectrometer at Utrecht University. Apart from samples, we measured additional carbonate standards in an approximate 1:1 ratio. To correct the sample measurements, we employed three standards (ETH-1, 2, and 3 in a 1:1:5 ratio respecitvely[103]), which differ in $\delta^{13}C$, $\delta^{18}O$, and Δ_{47} composition. Two additional check standards (IAEA-C2 and Merck) were measured to monitor the long-term reproducibility of the instrument. External reproducibility (one standard deviation) in Δ_{47} of IAEA-C2 after correction was 0.036‰. The $\delta^{13}C$ and $\delta^{18}O$ values (reported relative to the VPDB scale) of IAEA-C2 shows an external reproducibility (one standard deviation) of respectively 0.11 and 0.05‰.

Temperature and $\delta^{18}O_{sw}$ calculations. To determine clumped isotope-based deep-sea temperatures from the three averaged final corrected Δ_{47} values (background, slope, and hyperthermal peak), we employed a recent foraminifer-based calibration[49] recalculated to the InterCarb-Carbon Dioxide Equilibrium Scale (I-CDES) using the newly accepted values of the carbonate standards of ref 55.

$$\Delta_{47}(I-CDES_{90°C}) = 0.0397 \pm 0.0011 * \frac{10^6}{T^2} + 0.1518 \pm 0.0128 \; (T \; in \; K) \quad (1)$$

This Δ_{47}-temperature relationship represents a composite of previously published foraminifer based-calibrations[47,48] with new foraminiferal data[49], and has a larger data density in the range of ocean temperatures compared to other calibrations. Within uncertainty, this regression is indistinguishable from calibrations based on inorganic calcite[46,54].

Calculation of the $\delta^{18}O_b$-based deep-sea temperatures follows the approach that is used in the well-known reconstruction of ref 31 (see discussion in refs 31, 79). First, we converted $\delta^{18}O$ of *O. umbonatus* and *N. truempyi* towards *Cibicoides* values for assumed seawater equilibrium using the following correction factors from ref 29:

$$\delta^{18}O_{Cib} = \frac{\delta^{18}O_{Nutt} + 0.10}{0.89} \quad (2)$$

$$\delta^{18}O_{Cib} = \delta^{18}O_{Orid} - 0.28 \quad (3)$$

Subsequently, we determined deep-sea temperatures following the $\delta^{18}O_b$-temperature relationship of *Cibicoides*. In our study, we applied the recent improved calibration for *Cibicoides* of ref 79, which is based on a large data set existing of both previous and new core top measurements:

$$\delta^{18}O_b[‰VPBD] - \delta^{18}O_{sw}[‰VSMOW] + 0.27$$
$$= -0.245 \pm 0.005 * T + 0.0011 \pm 0.0002 * T^2 + 3.58 \pm 0.02 \ (T \text{ in } °C) \quad (4)$$

This quadratic regression shows good agreement with the regression of ref 104, which is based on inorganic calcite precipitated between 10 and 40 °C[77,104].

Finally, the translated *Cibicidoides* $\delta^{18}O_b$ values and the reconstructed Δ_{47}-based deep-sea temperatures were used in equation (2) to calculate the $\delta^{18}O_{sw}$, which allows for testing the traditional assumptions on $\delta^{18}O_{sw}$ in an ice-free world. We used the average $\delta^{18}O_b$ and average temperatures of the three states (background, slope, and hyperthermal peak) to calculate the three corresponding $\delta^{18}O_{sw}$ values. For our data representation and visualization, we show separate analytical and calibration uncertainties in the Δ_{47}- and $\delta^{18}O_b$ temperatures to indicate how much of the uncertainty is contained in the analytical measurement performance and in the calibration. The analytical and calibration uncertainty also act differently on the reconstructed temperatures. For instance regarding the Δ_{47}- based temperatures, the analytical uncertainty is different for each of these three 3 bins and would affect the temperature difference between hyperthermal and background Eocene conditions, while the calibration uncertainty would influence the temperatures of these three bins in one direction at the same time (e.g. baseline shift, increase or decrease temperature of all three bins).

Data availability In case our manuscript is accepted, the clumped and stable isotope data of this study will be made available on the open access data repository EarthChem.

References

1. Anagnostou, E. *et al*. Changing atmospheric CO_2 concentration was the primary driver of early Cenozoic climate. *Nature* **533**, 380-384 (2016).

2. Anagnostou, E. *et al*. Proxy evidence for state-dependence of climate sensitivity in the Eocene greenhouse. *Nature communications* **11**, 1–9 (2020).
3. Zachos, J., Pagani, M., Sloan, L., Thomas, E. & Billups, K. Trends, rhythms, and aberrations in global climate 65 Ma to present. *Science* **292**, 686–693 (2001).
4. Zachos, J. C., Dickens, G. R. & Zeebe, R. E. An early Cenozoic perspective on greenhouse warming and carbon-cycle dynamics. *Nature* **451**, 279–283 (2008).
5. Sluijs, A. *et al*. Subtropical Arctic Ocean temperatures during the Palaeocene/Eocene thermal maximum. *Nature* **441**, 610-613 (2006).
6. Bijl, P. K. *et al*. Early Palaeogene temperature evolution of the southwest Pacific Ocean. *Nature* **461**, 776-779 (2009).
7. Cramwinckel, M. J. *et al*. Synchronous tropical and polar temperature evolution in the Eocene. *Nature* **559**, 382-386 (2018).
8. Hollis, C. J. *et al*. The DeepMIP contribution to PMIP4: methodologies for selection, compilation and analysis of latest Paleocene and early Eocene climate proxy data, incorporating version 0.1 of the DeepMIP database. *Geoscientific Model Development* **12**, 3149-3206 (2019).
9. Inglis, G. N. *et al*. Global mean surface temperature and climate sensitivity of the early Eocene Climatic Optimum (EECO), Paleocene–Eocene Thermal Maximum (PETM), and latest Paleocene. *Climate of the Past* **16**, 1953-1968 (2020).
10. Westerhold, T. *et al*. An astronomically dated record of Earth's climate and its predictability over the last 66 million years. *Science* **369**, 1383-1387 (2020).
11. Burke, K. D. *et al*. Pliocene and Eocene provide best analogs for near-future climates. *Proceedings of the National Academy of Sciences* **115**, 13288-13293 (2018).
12. Lear, C. H., Elderfield, H. & Wilson, P. A. Cenozoic deep-sea temperatures and global ice volumes from Mg/Ca in benthic foraminiferal calcite. *Science* **287**, 269-272 (2000).
13. PALAEOSENS Project Members. Making sense of palaeoclimate sensitivity. *Nature* **491**, 683–691 (2012).
14. Hansen, J., Sato, M., Russell, G. & Kharecha, P. Climate sensitivity, sea level and atmospheric carbon dioxide. *Philosophical Transactions of the Royal Society A: Mathematical, Physical and Engineering Sciences* **371**, 20120294 (2013).
15. Valdes, P. J., Scotese, C. R. & Lunt, D. J. Deep ocean temperatures through time. *Climate of the Past Discussions*, 1-37 (2020).
16. Sexton, P. F. *et al*. Eocene global warming events driven by ventilation of oceanic dissolved organic carbon. *Nature* **471**, 349-352 (2011).
17. Turner, S. K., Sexton, P. F., Charles, C. D. & Norris, R. D. Persistence of carbon release events through the peak of early Eocene global warmth. *Nature Geoscience* **7**, 748-751 (2014).

18. Lauretano, V., Zachos, J. C. & Lourens, L. J. Orbitally paced carbon and deep-sea temperature changes at the peak of the early Eocene climatic optimum. *Paleoceanography and Paleoclimatology* **33**, 1050–1065 (2018).
19. Westerhold, T., Röhl, U., Donner, B. & Zachos, J. C. Global extent of early Eocene hyperthermal events: A new Pacific benthic foraminiferal isotope record from Shatsky Rise (ODP Site 1209). *Paleoceanography and Paleoclimatology* **33**, 626-642 (2018).
20. Dickens, G. R., O'Neil, J. R., Rea, D. K. & Owen, R. M. Dissociation of oceanic methane hydrate as a cause of the carbon isotope excursion at the end of the Paleocene. *Paleoceanography* **10**, 965-971 (1995).
21. Dickens, G. R., Castillo, M. M. & Walker, J. C. A blast of gas in the latest Paleocene: Simulating first-order effects of massive dissociation of oceanic methane hydrate. *Geology* **25**, 259-262 (1997).
22. DeConto, R. M. *et al*. Past extreme warming events linked to massive carbon release from thawing permafrost. *Nature* **484**, 87-91 (2012).
23. Ravelo, A. C. & Hillaire-Marcel, C. Chapter eighteen the use of oxygen and carbon isotopes of foraminifera in paleoceanography. *Developments in marine geology* **1**, 735-764 (2007).
24. Pearson, P. N. Oxygen isotopes in foraminifera: Overview and historical review. *The Paleontological Society Papers* **18**, 1–38 (2012).
25. Shackleton, N. J. Paleogene stable isotope events. *Palaeogeogr. , Palaeoclimatol. , Palaeoecol.* **57**, 91-102 (1986).
26. Spero, H. J., Bijma, J., Lea, D. W. & Bemis, B. E. Effect of seawater carbonate concentration on foraminiferal carbon and oxygen isotopes. *Nature* **390**, 497–500 (1997).
27. Zeebe, R. E. An explanation of the effect of seawater carbonate concentration on foraminiferal oxygen isotopes. *Geochim. Cosmochim. Acta* **63**, 2001-2007 (1999).
28. Zeebe, R. E. Seawater pH and isotopic paleotemperatures of Cretaceous oceans. *Palaeogeogr. , Palaeoclimatol. , Palaeoecol.* **170**, 49-57 (2001).
29. Katz, M. E. *et al*. Early Cenozoic benthic foraminiferal isotopes: Species reliability and interspecies correction factors. *Paleoceanography* **18,** (2003).
30. Tripati, A. & Elderfield, H. Deep-sea temperature and circulation changes at the Paleocene-Eocene thermal maximum. *Science* **308**, 1894–1898 (2005).
31. Cramer, B. S., Miller, K. G., Barrett, P. J. & Wright, J. D. Late Cretaceous–Neogene trends in deep ocean temperature and continental ice volume: Reconciling records of benthic foraminiferal geochemistry (δ18O and Mg/Ca) with sea level history. *Journal of Geophysical Research: Oceans* **116,** (2011).
32. Evans, D. & Müller, W. Deep time foraminifera Mg/Ca paleothermometry: Nonlinear correction for secular change in seawater Mg/Ca. *Paleoceanography* **27** (2012).

33. Coggon, R. M., Teagle, D. A., Smith-Duque, C. E., Alt, J. C. & Cooper, M. J. Reconstructing past seawater Mg/Ca and Sr/Ca from mid-ocean ridge flank calcium carbonate veins. *Science* **327**, 1114-1117 (2010).
34. Lear, C. H. *et al*. Neogene ice volume and ocean temperatures: Insights from infaunal foraminiferal Mg/Ca paleothermometry. *Paleoceanography* **30**, 1437-1454 (2015).
35. Evans, D. *et al*. Eocene greenhouse climate revealed by coupled clumped isotope-Mg/Ca thermometry. *Proceedings of the National Academy of Sciences* **115**, 1174-1179 (2018).
36. Miller, K. G. *et al*. Cenozoic sea-level and cryospheric evolution from deep-sea geochemical and continental margin records. *Science advances* **6**, eaaz1346 (2020).
37. Elderfield, H., Yu, J., Anand, P., Kiefer, T. & Nyland, B. Calibrations for benthic foraminiferal Mg/Ca paleothermometry and the carbonate ion hypothesis. *Earth Planet. Sci. Lett.* **250**, 633-649 (2006).
38. Rosenthal, Y., Lear, C. H., Oppo, D. W. & Linsley, B. K. Temperature and carbonate ion effects on Mg/Ca and Sr/Ca ratios in benthic foraminifera: Aragonitic species Hoeglundina elegans. *Paleoceanography* **21** (2006).
39. Marchitto, T. M., Bryan, S. P., Curry, W. B. & McCorkle, D. C. Mg/Ca temperature calibration for the benthic foraminifer Cibicidoides pachyderma. *Paleoceanography* **22** (2007).
40. Bryan, S. P., & Marchitto, T. M. (2008). Mg/ca–temperature proxy in benthic foraminifera: New calibrations from the florida straits and a hypothesis regarding mg/li. *Paleoceanography, 23*(2)
41. Lear, C. H., Mawbey, E. M. & Rosenthal, Y. Cenozoic benthic foraminiferal Mg/Ca and Li/Ca records: Toward unlocking temperatures and saturation states. *Paleoceanography* **25** (2010).
42. Evans, D., Wade, B. S., Henehan, M., Erez, J. & Müller, W. Revisiting carbonate chemistry controls on planktic foraminifera Mg/Ca: implications for sea surface temperature and hydrology shifts over the Paleocene–Eocene Thermal Maximum and Eocene–Oligocene transition. *Climate of the Past* **12**, 819-835 (2016).
43. Tripati, A. K. *et al*. 13C–18O isotope signatures and 'clumped isotope'thermometry in foraminifera and coccoliths. *Geochim. Cosmochim. Acta* **74**, 5697–5717 (2010).
44. Tripati, A. K. *et al*. Beyond temperature: Clumped isotope signatures in dissolved inorganic carbon species and the influence of solution chemistry on carbonate mineral composition. *Geochim. Cosmochim. Acta* **166**, 344-371 (2015).
45. Grauel, A. *et al*. Calibration and application of the 'clumped isotope'thermometer to foraminifera for high-resolution climate reconstructions. *Geochim. Cosmochim. Acta* **108**, 125–140 (2013).
46. Kele, S. *et al*. Temperature dependence of oxygen-and clumped isotope fractionation in carbonates: a study of travertines and tufas in the 6–95 C temperature range. *Geochim. Cosmochim. Acta* **168**, 172-192 (2015).
47. Peral, M. *et al*. Updated calibration of the clumped isotope thermometer in planktonic and benthic foraminifera. *Geochim. Cosmochim. Acta* **239**, 1–16 (2018).

48. Piasecki, A. *et al*. Application of clumped isotope thermometry to benthic foraminifera. *Geochem. Geophys. Geosyst.* **20**, 2082–2090 (2019).
49. Meinicke, N. *et al*. A robust calibration of the clumped isotopes to temperature relationship for foraminifers. *Geochim. Cosmochim. Acta* **270**, 160–183 (2020).
50. Anderson, N. T. *et al*. A Unified Clumped Isotope Thermometer Calibration (0.5–1,100° C) Using Carbonate-Based Standardization. *Geophys. Res. Lett.* **48**, e2020GL092069 (2021).
51. Ghosh, P. *et al*. 13C–18O bonds in carbonate minerals: a new kind of paleothermometer. *Geochim. Cosmochim. Acta* **70**, 1439-1456 (2006).
52. Eiler, J. M. "Clumped-isotope" geochemistry—The study of naturally-occurring, multiply-substituted isotopologues. *Earth Planet. Sci. Lett.* **262**, 309-327 (2007).
53. Eiler, J. M. Paleoclimate reconstruction using carbonate clumped isotope thermometry. *Quaternary Science Reviews* **30**, 3575-3588 (2011).
54. Bernasconi, S. M. *et al*. Reducing uncertainties in carbonate clumped isotope analysis through consistent carbonate-based standardization. *Geochem. Geophys. Geosyst.* **19**, 2895–2914 (2018).
55. Bernasconi, S. M. *et al*. InterCarb: A community effort to improve interlaboratory standardization of the carbonate clumped isotope thermometer using carbonate standards. *Geochem. Geophys. Geosyst.* **22**, e2020GC009588 (2021).
56. Schmid, T. W. & Bernasconi, S. M. An automated method for 'clumped-isotope'measurements on small carbonate samples. *Rapid Communications in Mass Spectrometry* **24**, 1955-1963 (2010).
57. Hu, B. *et al*. A modified procedure for gas-source isotope ratio mass spectrometry: The long-integration dual-inlet (LIDI) methodology and implications for clumped isotope measurements. *Rapid Communications in Mass Spectrometry* **28**, 1413–1425 (2014).
58. Meckler, A. N., Ziegler, M., Millán, M. I., Breitenbach, S. F. & Bernasconi, S. M. Long-term performance of the Kiel carbonate device with a new correction scheme for clumped isotope measurements. *Rapid Communications in Mass Spectrometry* **28**, 1705–1715 (2014).
59. Müller, I. A. *et al*. Carbonate clumped isotope analyses with the long-integration dual-inlet (LIDI) workflow: Scratching at the lower sample weight boundaries. *Rapid Communications in Mass Spectrometry* **31**, 1057–1066 (2017).
60. Tripati, A. K. *et al*. Modern and glacial tropical snowlines controlled by sea surface temperature and atmospheric mixing. *Nature Geoscience* **7**, 205-209 (2014).
61. Thornalley, D. J. *et al*. A warm and poorly ventilated deep Arctic Mediterranean during the last glacial period. *Science* **349**, 706-710 (2015).
62. Rodríguez-Sanz, L. *et al*. Penultimate deglacial warming across the Mediterranean Sea revealed by clumped isotopes in foraminifera. *Scientific Reports* **7**, 1–11 (2017).

63. Leutert, T. J. *et al*. Sensitivity of clumped isotope temperatures in fossil benthic and planktic foraminifera to diagenetic alteration. *Geochim. Cosmochim. Acta* **257**, 354–372 (2019).
64. Leutert, T. J., Auderset, A., Martínez-García, A., Modestou, S. & Meckler, A. N. Coupled Southern Ocean cooling and Antarctic ice sheet expansion during the middle Miocene. *Nature Geoscience* **13**, 634–639 (2020).
65. Leutert, T. J., Modestou, S., Bernasconi, S. M. & Meckler, A. N. Southern Ocean bottom water cooling and ice sheet expansion during the middle Miocene climate transition. *Climate of the Past Discussions*, 1–26 (2020).
66. Modestou, S. E., Leutert, T. J., Fernandez, A., Lear, C. H. & Meckler, A. N. Warm middle Miocene Indian Ocean bottom water temperatures: Comparison of clumped isotope and Mg/Ca-based estimates. *Paleoceanography and Paleoclimatology* **35**, e2020PA003927 (2020).
67. Evans, D. Deep heat: proxies, Miocene ice, and an end in sight for paleoclimate paradoxes? *Paleoceanography and Paleoclimatology* **36**, e2020PA004174 (2021).
68. Lourens, L. J. *et al*. Astronomical pacing of late Palaeocene to early Eocene global warming events. *Nature* **435**, 1083–1087 (2005).
69. Stap, L. *et al*. High-resolution deep-sea carbon and oxygen isotope records of Eocene Thermal Maximum 2 and H2. *Geology* **38**, 607–610 (2010).
70. Kennett, J. P. & Stott, L. D. Abrupt deep-sea warming, palaeoceanographic changes and benthic extinctions at the end of the Palaeocene. *Nature* **353**, 225–229 (1991).
71. Zachos, J. C. *et al*. Rapid acidification of the ocean during the Paleocene-Eocene thermal maximum. *Science* **308**, 1611–1615 (2005).
72. de Winter, N., Agterhuis, T. & Ziegler, M. Optimizing sampling strategies in high-resolution paleoclimate records. *Climate of the Past Discussions*, 1-52 (2020).
73. Shackleton, N. J. Attainment of isotopic equilibrium between ocean water and the benthonic foraminifera genus Uvigerina: Isotopic changes in the ocean during the last glacial. *Colloq. Int. C. N. R. S.* **219**, 203–209 (1974).
74. Graham, D. W., Corliss, B. H., Bender, M. L. & Keigwin Jr, L. D. Carbon and oxygen isotopic disequilibria of recent deep-sea benthic foraminifera. *Mar. Micropaleontol.* **6**, 483-497 (1981).
75. Shackleton, N. J., Hall, M. A. & Boersma, A. Oxygen and carbon isotope data from Leg 74 foraminifers. *Init. Rep. Deep Sea Drill. Proj*. **74**, 599 – 612 (1984).
76. Shackleton, N. J. &Hall, M. A. The late Miocene stable isotope record, Site 926. *Proc. Ocean Drill. Prog. Sci. Results*. **154**, 367 – 373 (1997).
77. Bemis, B. E., Spero, H. J., Bijma, J. & Lea, D. W. Reevaluation of the oxygen isotopic composition of planktonic foraminifera: Experimental results and revised paleotemperature equations. *Paleoceanography* **13**, 150–160 (1998).

78. Lynch-Stieglitz, J., Curry, W. B. & Slowey, N. A geostrophic transport estimate for the Florida Current from the oxygen isotope composition of benthic foraminifera. *Paleoceanography* **14**, 360-373 (1999).
79. Marchitto, T. M. *et al*. Improved oxygen isotope temperature calibrations for cosmopolitan benthic foraminifera. *Geochim. Cosmochim. Acta* **130**, 1–11 (2014).
80. Pross, J. *et al*. Persistent near-tropical warmth on the Antarctic continent during the early Eocene epoch. *Nature* **488**, 73-77 (2012).
81. Willard, D. A. *et al*. Arctic vegetation, temperature, and hydrology during Early Eocene transient global warming events. *Global Planet. Change* **178**, 139-152 (2019).
82. Tripati, A., Backman, J., Elderfield, H. & Ferretti, P. Eocene bipolar glaciation associated with global carbon cycle changes. *Nature* **436**, 341-346 (2005).
83. Stickley, C. E. *et al*. Evidence for middle Eocene Arctic sea ice from diatoms and ice-rafted debris. *Nature* **460**, 376-379 (2009).
84. Tripati, A. & Darby, D. Evidence for ephemeral middle Eocene to early Oligocene Greenland glacial ice and pan-Arctic sea ice. *Nature communications* **9**, 1-11 (2018).
85. Lunt, D. J. *et al*. CO2-driven ocean circulation changes as an amplifier of Paleocene-Eocene thermal maximum hydrate destabilization. *Geology* **38**, 875–878 (2010).
86. Cramer, B. S., Toggweiler, J. R., Wright, J. D., Katz, M. E. & Miller, K. G. Ocean overturning since the Late Cretaceous: Inferences from a new benthic foraminiferal isotope compilation. *Paleoceanography* **24,** (2009).
87. Wendler, J. E., Wendler, I., Vogt, C. & Kuss, J. Link between cyclic eustatic sea-level change and continental weathering: Evidence for aquifer-eustasy in the Cretaceous. *Palaeogeogr. , Palaeoclimatol. , Palaeoecol.* **441**, 430-437 (2016).
88. Sames, B., Wagreich, M., Conrad, C. P. & Iqbal, S. Aquifer-eustasy as the main driver of short-term sea-level fluctuations during Cretaceous hothouse climate phases. *Geological Society, London, Special Publications* **498**, 9-38 (2020).
89. Davies, A. *et al*. Assessing the impact of aquifer-eustasy on short-term Cretaceous sea-level. *Cretaceous Res.* **112**, 104445 (2020).
90. Wallmann, K. The geological water cycle and the evolution of marine δ18O values. *Geochim. Cosmochim. Acta* **65**, 2469-2485 (2001).
91. Jaffrés, J. B., Shields, G. A. & Wallmann, K. The oxygen isotope evolution of seawater: A critical review of a long-standing controversy and an improved geological water cycle model for the past 3.4 billion years. *Earth-Sci. Rev.* **83**, 83-122 (2007).
92. Kominz, M. A. Oceanic ridge volumes and sea-level change - an error analysis. Am. J. Petrol. Geol. Mem. **36**, 109-127 (1984).

526 93. Conrad, C. P. & Lithgow-Bertelloni, C. Faster seafloor spreading and lithosphere production during the mid-
527 Cenozoic. *Geology* **35**, 29-32 (2007).
528 94. Raitzsch, M. & Hönisch, B. Cenozoic boron isotope variations in benthic foraminifers. *Geology* **41**, 591-594
529 (2013).
530 95. Uchikawa, J. & Zeebe, R. E. Examining possible effects of seawater pH decline on foraminiferal stable
531 isotopes during the Paleocene-Eocene Thermal Maximum. *Paleoceanography* **25,** (2010).
532 96. Tripati, A. K. *et al*. Beyond temperature: Clumped isotope signatures in dissolved inorganic carbon species
533 and the influence of solution chemistry on carbonate mineral composition. *Geochim. Cosmochim. Acta* **166**,
534 344-371 (2015).
535 97. Guo, W. Kinetic clumped isotope fractionation in the DIC-H2O-CO2 system: patterns, controls, and
536 implications. *Geochim. Cosmochim. Acta* **268**, 230-257 (2020).
537 98. McCarren, H., Thomas, E., Hasegawa, T., Röhl, U. & Zachos, J. C. Depth dependency of the Paleocene-
538 Eocene carbon isotope excursion: Paired benthic and terrestrial biomarker records (Ocean Drilling Program
539 Leg 208, Walvis Ridge). *Geochem. Geophys. Geosyst.* **9** (2008).
540 99. Stolper, D. A., Eiler, J. M. & Higgins, J. A. Modeling the effects of diagenesis on carbonate clumped-isotope
541 values in deep-and shallow-water settings. *Geochim. Cosmochim. Acta* **227**, 264–291 (2018).
542 100. Edgar, K. M., Pälike, H. & Wilson, P. A. Testing the impact of diagenesis on the δ18O and δ13C of benthic
543 foraminiferal calcite from a sediment burial depth transect in the equatorial Pacific. *Paleoceanography* **28**, 468–
544 480 (2013).
545 101. Voigt, J., Hathorne, E. C., Frank, M., Vollstaedt, H. & Eisenhauer, A. Variability of carbonate diagenesis in
546 equatorial Pacific sediments deduced from radiogenic and stable Sr isotopes. *Geochim. Cosmochim. Acta* **148**,
547 360–377 (2015).
548 102. Voigt, J., Hathorne, E. C., Frank, M. & Holbourn, A. Minimal influence of recrystallization on middle Miocene
549 benthic foraminiferal stable isotope stratigraphy in the eastern equatorial Pacific. *Paleoceanography* **31**, 98–
550 114 (2016).
551 103. Kocken, I. J., Müller, I. A. & Ziegler, M. Optimizing the use of carbonate standards to minimize uncertainties
552 in clumped isotope data. *Geochem. Geophys. Geosyst.* **20**, 5565–5577 (2019).
553 104. Kim, S. & O'Neil, J. R. Equilibrium and nonequilibrium oxygen isotope effects in synthetic carbonates. *Geochim.*
554 *Cosmochim. Acta* **61**, 3461–3475 (1997).
555 105. Westerhold, T. *et al*. Astronomical calibration of the Ypresian timescale: implications for seafloor spreading
556 rates and the chaotic behavior of the solar system? *Climate of the Past* **13,** (2017).
557

558 **Acknowledgements** This research was conducted under the program of the Netherlands Earth System Science
559 Centre (NESSC), financially supported by the Ministry of Education, Culture and Sciences (OCW) of the

Netherlands. M. Ziegler acknowledges additional support from NWO research grant 016.161.365. This work used samples and data provided by the Ocean Drilling Program (ODP). We thank I.J. Kocken (Utrecht University) for processing the raw clumped isotope data in R, and A. E. van Dijk (Utrecht Geolab) for technical support in the lab.

Author contributions T.A., M.Z., and L.J.L. designed the study. T.A. generated the stable and clumped isotope data. All authors contributed to data interpretation and the written manuscript.

Competing interests The authors declare no competing interests.

Materials and correspondence requests should be addressed to T.A.

Extended data

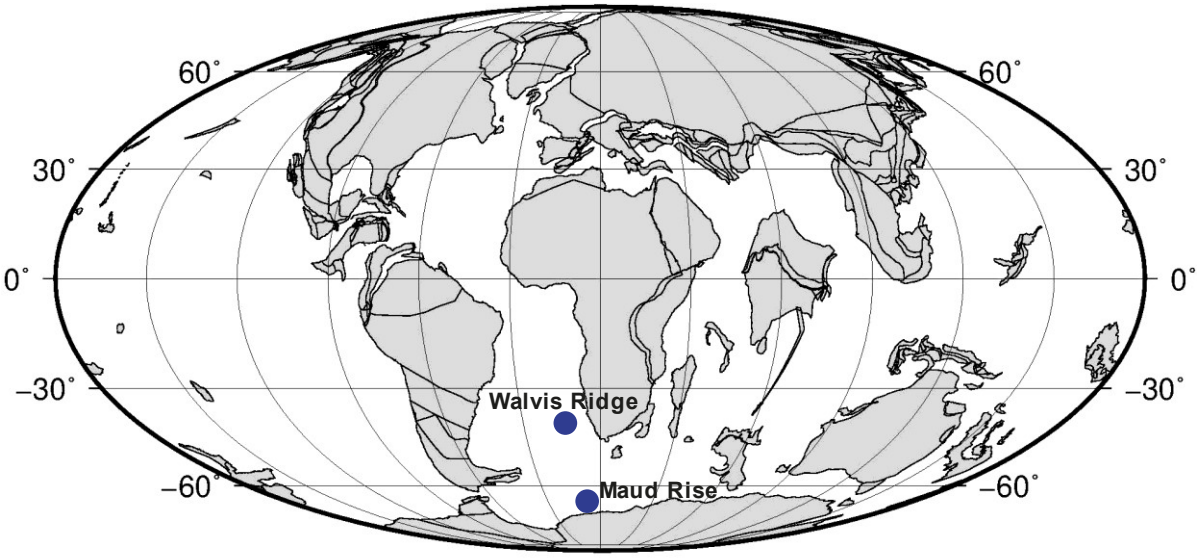

Extended Data Fig. 1 | Paleogeographic reconstruction (54.0 Ma) with location of Walvis Ridge and Maud Rise. This map is generated from the plate tectonic reconstruction service of the Ocean Drilling Stratigraphic Network (ODSN; http://www.odsn.de)..

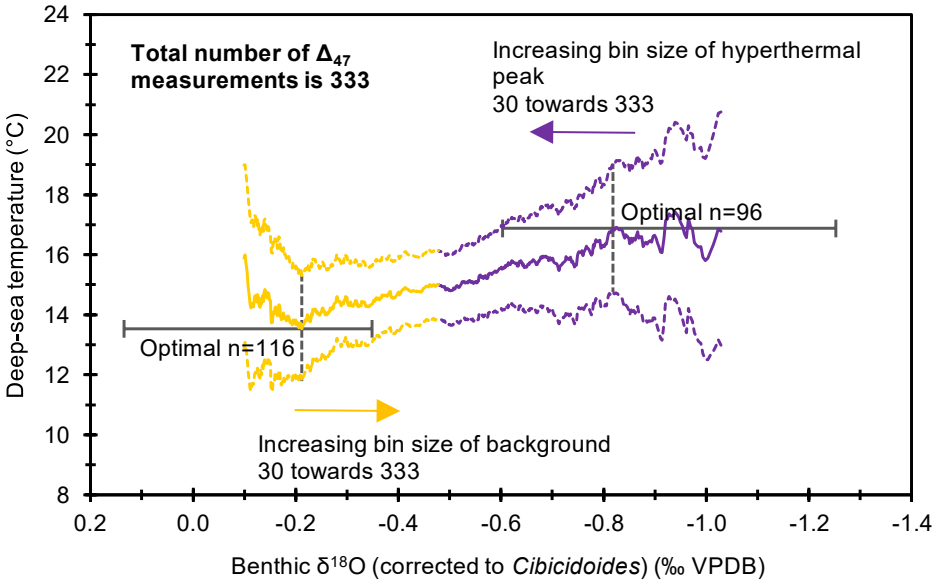

Extended Data Fig. 2 | Background and hyperthermal peak temperatures (mean and 95% CI) as a function of bin size. Adding Δ_{47} measurements with progressively lower and higher $\delta^{18}O$ values results in increasing bin sizes of the background (orange) and hyperthermal peak (purple) states respectively. The mean values of these two bins move towards each other with increasing bin size. The 95% CI decreases with increasing bin size. A size of 116 and 96 Δ_{47} measurements for the background and hyperthermal peak bins respectively yields the most significant difference between the two populations. See ref 72 for further details on this approach.

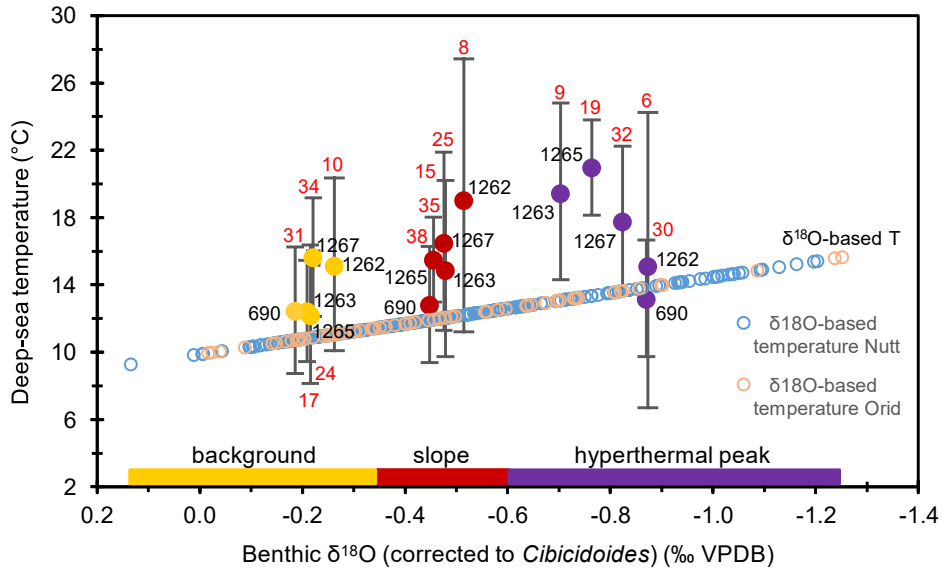

Extended Data Fig. 3 | The compiled Δ_{47}-based temperature bins (background, slope and hyperthermal peak) deconvolved into data per site (mean and 95% CI). The variability in the temperatures among the sites can attributed to limited measurements. Deep-sea temperatures at Site 690 though seem to be slightly cooler in comparison to the Walvis Ridge sites. However, it is not possible to state this with confidence due to the uncertainty in the temperature estimates.

Extended Data Table 1 | Optimal Δ_{47} bin sizes. Overview of the 30 most optimal bin sizes for the background and hyperthermal peak Δ_{47} populations determined using a Welch t-test, i.e., the bin sizes that result in the most significant difference (lowest p-values).

Δ_{47} bin size background	Δ_{47} bin size hyperthermal peak	Lowest p-values
116	96	0.0191
116	93	0.0199
116	97	0.0204
116	94	0.0204
116	99	0.0214
111	96	0.0215
116	92	0.0216
116	95	0.0218
111	93	0.0223
118	96	0.0229
111	94	0.0229
111	97	0.0230
116	98	0.0230
117	96	0.0237
118	93	0.0238
111	99	0.0241
111	92	0.0242
116	100	0.0243
116	91	0.0243
118	94	0.0244
118	97	0.0244
111	95	0.0244
119	96	0.0245
117	93	0.0246
115	96	0.0247
116	55	0.0249
117	94	0.0253
117	97	0.0253
119	93	0.0254
120	96	0.0255

Supplementary Information

Mass spectrometry and clumped isotope data processing

In total, we carried out 27 runs with each of them containing 22 samples (sometimes also containing samples of other projects) interspersed with 24 carbonate standards, over a period of one year. We randomized the distribution of the samples over this period to prevent biases in the obtained data due to variability and longer-term trends in the mass spectrometer performance. The relative proportions of the measured standards ETH-1:ETH-2:ETH-3 was 1:1:5, as optimal minimization of uncertainties in the Δ_{47} data is achieved by measuring relatively more ETH-3 (ref 1). In the *Thermo Scientific Kiel IV* device, the carbonate material was digested with phosphoric acid (H_3PO_4) at a reaction temperature of 70 °C (ref 2). Steps were subsequently taken in the instrument to purify the sample gas. First, the gas was transported to a first cryogenic liquid nitrogen (LN_2) trap with a temperature of –196 °C. Here, CO_2 and H_2O amongst others were frozen and trapped while non-condensable gases (originating from impurities in the sample) were removed[2]. The gas was then transferred through a Porapak-Q trap cooled at –40 °C to remove organic contaminants, such as halo-/hydrocarbons and reduced sulfur compounds[2]. After a second cold trap a near pure CO_2 gas remained, which was sent into the *Thermo Scientific MAT 253 Plus* instrument for isotope analysis. The mass spectrometer collected the signals of m/z 44–49 of the gas, which correspond with the different isotopologues of CO_2 (refs 2,3). The m/z 48 and 49 signals were used to detect potential contamination[4]. To obtain the necessary accuracy of the measurements, the sample gas was measured against a reference gas of known isotopic composition ($\delta^{13}C$ = –2.82‰; $\delta^{18}O$ = –4.67‰)[5,6]. Measurements with the mass spectrometer were done in micro-volume and followed the long-integration dual-inlet (LIDI) method[6,7].

We applied a pressure sensitive baseline correction (PBL) to correct the obtained data for negative backgrounds using peak scans at m/z 44 intensities of 5, 10, 15, 20, and 25 V, which were performed during run preparation[4,8,9]. Subsequently, the ETH-1, ETH-2, and ETH-3 standards were used to correct sample Δ_{47} data and normalize it into the InterCarb-Carbon Dioxide Equilibrium Scale (I-CDES)[10,11,12], to correct for offsets in $\delta^{13}C$ and $\delta^{18}O$, and to correct for scale compression/stretching in $\delta^{18}O$. We applied an offset correction based on two neighboring ETH-3 standards to correct the Δ_{47} sample measurements for long-term variability in the mass spectrometer performance. Then, the data was transferred into the I-CDES by using an empirical transfer function (ETF) that is based on the raw Δ_{47} values of the ETH standards of a window of 4 runs and their InterCarb accepted values at 90 °C acid reaction temperature as determined by ref 12 (ETH-1: Δ_{47} = 0.2052±0.0016‰ (1SE); ETH-2: Δ_{47} = 0.2085±0.0015‰ (1SE); ETH-3: Δ_{47} = 0.6132±0.0014‰ (1SE). To determine final values for both $\delta^{13}C$ and $\delta^{18}O$, an offset correction was applied based on the measured and reported stable isotope values of all three ETH standards in ref 11 (ETH-1: $\delta^{13}C_{VPDB}$ = 2.02±0.03‰, $\delta^{18}O_{VPDB}$ = –2.19±0.04‰; ETH-2: $\delta^{13}C_{VPDB}$ = –10.17±0.06‰, $\delta^{18}O_{VPDB}$ = –18.69±0.11‰; ETH-3: $\delta^{13}C_{VPDB}$ = 1.71±0.02‰, $\delta^{18}O_{VPDB}$ = –1.78±0.06‰).

The external reproducibility (one standard deviation) of the $\delta^{13}C$, $\delta^{18}O$, and Δ_{47} measurements for each of the standards is listed in the Archive in the Supplementary Data File. External reproducibility (one standard deviation) in Δ_{47} of all the carbonate standards after correction was typically 0.030–0.040‰. The $\delta^{13}C$ and $\delta^{18}O$ values (reported relative to the VPDB scale) of the standards show an external reproducibility (one standard deviation) of respectively 0.10 and 0.05‰ on average. Regarding the clumped isotope data, outliers are absent in the successful (no issues with backgrounds, contamination, and/or intensity) sample measurements. The final Δ_{47} values of all these successful measurements are within 4 standard deviations off from the mean. Raw stable and clumped isotope data for all standard and sample measurements are included in the Supplementary Data File.

References

1. Kocken, I. J., Müller, I. A. & Ziegler, M. Optimizing the use of carbonate standards to minimize uncertainties in clumped isotope data. *Geochem. Geophys. Geosyst.* **20**, 5565–5577 (2019).
2. Schmid, T. W., Radke, J. & Bernasconi, S. M. Clumped-isotope measurements on small carbonate samples with a Kiel IV carbonate device and a MAT 253 mass spectrometer. *Thermo Fisher Application Note* **30233,** (2012).
3. Ghosh, P. *et al*. 13C–18O bonds in carbonate minerals: a new kind of paleothermometer. *Geochim. Cosmochim. Acta* **70**, 1439-1456 (2006).
4. Bernasconi, S. M. *et al*. Background effects on Faraday collectors in gas-source mass spectrometry and implications for clumped isotope measurements. *Rapid Communications in Mass Spectrometry* **27**, 603–612 (2013).
5. Huntington, K. W. *et al*. Methods and limitations of 'clumped'CO2 isotope (Δ47) analysis by gas-source isotope ratio mass spectrometry. *Journal of Mass Spectrometry* **44**, 1318–1329 (2009).
6. Müller, I. A. *et al*. Carbonate clumped isotope analyses with the long-integration dual-inlet (LIDI) workflow: Scratching at the lower sample weight boundaries. *Rapid Communications in Mass Spectrometry* **31**, 1057–1066 (2017).
7. Hu, B. *et al*. A modified procedure for gas-source isotope ratio mass spectrometry: The long-integration dual-inlet (LIDI) methodology and implications for clumped isotope measurements. *Rapid Communications in Mass Spectrometry* **28**, 1413–1425 (2014).
8. He, B., Olack, G. A. & Colman, A. S. Pressure baseline correction and high-precision CO2 clumped-isotope (Δ 47) measurements in bellows and micro-volume modes. *Rapid Communications in Mass Spectrometry* **26**, 2837–2853 (2012).

9. Meckler, A. N., Ziegler, M., Millán, M. I., Breitenbach, S. F. & Bernasconi, S. M. Long-term performance of the Kiel carbonate device with a new correction scheme for clumped isotope measurements. *Rapid Communications in Mass Spectrometry* **28**, 1705–1715 (2014).
10. Dennis, K. J., Affek, H. P., Passey, B. H., Schrag, D. P. & Eiler, J. M. Defining an absolute reference frame for 'clumped'isotope studies of CO2. *Geochim. Cosmochim. Acta* **75**, 7117–7131 (2011).
11. Bernasconi, S. M. *et al*. Reducing uncertainties in carbonate clumped isotope analysis through consistent carbonate-based standardization. *Geochem. Geophys. Geosyst.* **19**, 2895–2914 (2018).
12. Bernasconi, S. M. *et al*. InterCarb: A community effort to improve interlaboratory standardization of the carbonate clumped isotope thermometer using carbonate standards. *Geochem. Geophys. Geosyst.* **22**, e2020GC009588 (2021).